Supplementary Materials for

Prediction of a low-temperature N₂ dissociation catalyst exploiting near-IR–to–visible light nanoplasmonics

John Mark P. Martirez and Emily A. Carter

The PDF file includes:

Other Supplementary Material for this manuscript includes the following:
(available at advances.sciencemag.org/cgi/content/full/3/12/eaao4710/DC1)

- movie S1 (.mp4 format). DFT + D3 CI-NEB–predicted structures along pathway *a* (physical adsorption).
- movie S2 (.mp4 format). DFT + D3 CI-NEB–predicted structures along pathway *b* (reorientation).
- movie S3 (.mp4 format). DFT + D3 CI-NEB–predicted structures along pathway *c* (dissociation).
- data file S1. Atomic structure files.

Supplementary Text

Energy convergence with respect to active space size

To establish the convergence of the energies with respect to the active space size, we performed two tests: (*i*) convergence of the singlet-triplet energy as a function of metal cluster CAS size and (*ii*) convergence of the adsorption and reaction energies as a function of the CAS size defined by both the metal cluster and the N_2 molecule.

In fig. S6-A we show the convergence in the energy difference between $S = 0$ and 1 for the embedded bare cluster by extending the metal cluster CAS from (6e,6o) to (12e,12o). $S=0$ is consistently predicted to be the more stable or nearly degenerate with $S=1$ in all CAS sizes investigated. The energy difference between the two spin manifolds decreases with the CAS size as expected, because higher spins have greater number of configuration state functions (CSFs) for a given CAS size, which disproportionately increases with CAS size relative to lower spin manifolds. However, the additional configurations originating from the new orbitals eventually become increasingly less important, thus leading to energy convergence.

The metal clusters' CASs are composed of Mo $4d$ states, mostly exhibiting hybridization with the Au $6s$ states. For $S=1$, the two unpaired electrons are associated with two nearly pure Mo $4d$-derived states. In fig. S6-B, the orbitals in the orange boxes are the same orbitals found in CAS(6e,6o), additional occupied-virtual pairs are added as the CAS(*n*e,*n*o) size is increased, namely in green boxes for $n=8$, blue for $n=10$, and violet for $n=12$. We note that the occupation of the occupied and virtual orbitals added at $n=12$ are already nearly 2 and 0, respectively, specifically 1.99 and 0.02 for $S=0$, and 1.99 and 0.03 for $S=1$. These orbital occupations suggest that there is no significant contribution from the electronic configurations involving excitations from and to these orbitals in the linear CSF expansion of the wavefunctions, thus leading to very well converged relative energy at $n=12$, here within 0.045 eV (~1 kcal/mol) between $n=10$ and 12. Note that the embedded cluster DFT predicts $S_z=1$ to be more stable by -0.12 eV, in agreement with the prediction for the slab (-0.07 eV). Thus the emergence of $S=0$ as the more (or nearly equally) stable spin structure in emb-NEVPT2 is not an artifact of the embedded cluster model.

We also calculated adsorption and reaction energies from CAS(10e,10o), where as expected, the values are more exothermic or less endothermic than predicted by CAS(12e,12o) due in part to under-correlation of the gas-phase N_2 molecule at this smaller CAS size (table S5). To probe convergence, ideally our energies should also be compared to a larger CAS size, *e.g.*, CAS(14e,14o). However, using current implementations, calculations cannot be completed at the NEVPT2 level at a CAS larger than (12e,12o) for our system. We thus performed restricted active space self-consistent field or RASSCF (*73*) calculations using a combination of CAS and RAS, to provide the reference wavefunctions for NEVPT2 with an expanded active space. We conducted RASSCF for a reduced, fixed CAS size of (4e,4o), commonly referred to as RAS2, combined with occupied and virtual RAS, commonly referred to as RAS1 and RAS3, respectively. Active spaces with totals of (12e,12o) and (14e,14o) will be referred to as CAS(4e,4o)+RAS(8e,8o) and CAS(4e,4o)+RAS(10e,10o), respectively. The RAS1 and RAS3 orbitals are defined by the four or five lowest-lying occupied states and four or five highest-lying virtual states, respectively, identified from their complementary CASSCF CAS(12e,12o) and

CAS(14e,14o) orbitals. Excitations with only a maximum of four electrons out and into RAS1 and RAS3, respectively, are allowed (*i.e.,* up to quadruples in each spaces). Because RASSCF is more approximate than CASSCF, in table S5, CAS(4e,4o)+RAS(8e,8o) is compared to CAS(12e,12o) to establish the error introduced by the RAS approximation. A CAS(6e,6o)+RAS(6e,6o), also with the four-electron restrictions in RAS1 and RAS3, is calculated to probe convergence with respect to the RAS size. We then compare CAS(4e,4o)+RAS(10e,10o) against CAS(4e,4o)+RAS(8e,8o) to approximate the convergence error going from (12e,12o) to (14e,14o) active spaces. We note that a CAS(6e,6o)+RAS(8e,8o) cannot be successfully performed in the NEVPT2 level. This is also true for any combination of CAS and RAS sizes with CAS > (4e,4o), with a total active space of (14e,14o) and maximum of four-electron excitation restrictions within the RAS.

For the (12e,12o) active space, the RASSCF/NEVPT2 calculations exhibit good agreement with the CASSCF/NEVPT2 with absolute errors less than 0.2 eV, although the RASSCF with CAS(4e,4o)+RAS(8e,8o) does not converge for the transition state (structure 16) and slowly converges for the dissociated state (structure 19). The CAS(4e,4o)+RAS(10e,10o) agrees with the CAS(12e,12o) also within 0.2 eV, while comparison between CAS(4e,4o)+RAS(10e,10o) against CAS(4e,4o)+RAS(8e,8o) yields a slightly higher absolute deviation of 0.3 eV. The RASSCF with CAS(4e,4o)+RAS(10e,10o) also cannot properly converge for the transition state and poorly converges for the product state, which illustrate the inadequacy of RASSCF in describing the strongly bound state of N_2 on the metal cluster.

PI-RET rate

The goal of this section is to derive the dependence of the plasmon-induced resonance energy transfer (PI-RET) rate on the oscillator strength, f, of the surface acceptor transitions and the spectral properties of the plasmonic metal, starting from the classic Förster theory expression. The transition rate for an RET, w_{RET}, (s^{-1}) according to Förster theory (radiationless near-field dipole-dipole interaction) is

$$w_{\mathrm{RET}} = \frac{\Phi_D 9\kappa^2 c^4}{8\pi \tau_D R^6} \int I_D(\omega)\sigma_A(\omega) \frac{d\omega}{\varepsilon_r^2 \omega^4} \tag{S1}$$

where Φ_D and τ_D are the donor fluorescence quantum yield and radiative lifetime, respectively, $I_D(\omega)$ is the angular-frequency(ω)-dependent normalized fluorescence of the donor (in s/rad), $\sigma_A(\omega)$ is the absorption cross section of the acceptor (in cm^2), R is the distance between the two dipoles, κ is an orientation factor between the two dipoles, c is the speed of light in vacuum, and ε_r is the real part of the dielectric constant of the surrounding medium (*51, 52*). The term $\int I(\omega)\sigma_A(\omega) \frac{d\omega}{\varepsilon_r^2 \omega^4}$ defines the spectral overlap between the donor emission and acceptor absorption, scaled by the coupling factor $\kappa^2/(\varepsilon_r^2 R^6)$ (*52*).

Using Mie theory within the quasistatic field approximation, the dipole scattering cross-section of an LSPR for a spherical nanoparticle with radius a is

$$\sigma_{sca}(\omega) = \pi a^2 Q_{sca} = \frac{8\pi a^6 |\varepsilon_d|^2 \omega^4}{3c^4} \left| \frac{\varepsilon_m - \varepsilon_d}{\varepsilon_m + 2\varepsilon_d} \right|^2 \tag{S2}$$

where ε_m and ε_d are the ω-dependent complex dielectric constants of the metal and the surrounding medium, respectively (17). ε_m is known to be strongly ω-dependent. Q_{sca} is referred to as the scattering efficiency, which is the ratio of the scattering cross-section and the physical cross-section of the nanoparticle, πa^2. At the plasmon resonance peak, the scattering cross-section becomes much greater than the particle's physical cross-section. The expression for $\sigma_{sca}(\omega)$ originates from the plasmon-induced dipole moment expression

$$\mu_{\text{LSPR}} = \alpha E_0 = \frac{\varepsilon_m - \varepsilon_d}{\varepsilon_m + \chi\varepsilon_d} a^3 E_0 \tag{S3}$$

where E_0 is the electric field of the incident light, α is the polarizability, and the shape factor χ is 2 for a sphere (17).

Thus for a plasmonic donor, in the absence of a Stokes shift (red-shifted emission)(24, 51) due to primarily elastic scattering, we have

$$\frac{\Phi_D}{\tau_D} I_D(\omega) = \frac{\Phi_{sca}}{\tau_{sca}} I(\omega) = \Phi_{sca} \frac{\omega^2 \sigma_{sca}(\omega)}{\pi^2 c^2} \tag{S4}$$

because the radiative lifetime, τ, is related to the cross-section, σ, via

$$\sigma = \frac{\lambda^2}{8\pi\tau} I(\nu) = \frac{\lambda^2}{8\pi\tau} [2\pi I(\omega)] = \frac{\pi^2 c^2}{\omega^2 \tau} I(\omega) \tag{S5}$$

for a two-level system (74). λ and ν are the wavelength and frequency of the incident light, respectively. We thus approximate the metal as being a two-level donor (24). Here Φ_D and τ_D are redefined as the scattering quantum yield and lifetime of the LSPR, which are frequency dependent. By substituting Eqns. S2 and S4 into Eqn. S1, PI-RET transition rate becomes

$$w_{\text{RET}} = \frac{3\kappa^2}{\pi^2 c^2} \frac{a^6}{R^6} \int \Phi_{sca} \frac{|\varepsilon_d|^2}{\varepsilon_r^2} \left| \frac{\varepsilon_m - \varepsilon_d}{\varepsilon_m + 2\varepsilon_d} \right|^2 \omega^2 \sigma_A(\omega) d\omega \tag{S6}$$

Φ_{sca} may be approximated from the ratio of the scattering and extinction cross-sections of the LSPR (75). The expression above is similar to what is proposed in Ref. (51) for PI-RET between a metal and a semiconductor, in that they used the quasistatic field Mie theory expression for μ_{LSPR} in Ref. (17) to define the spectrum of the metal. However, instead of using the corresponding frequency-dependent scattering cross-section expression derived in Ref. (17), they evaluated the metal's spectrum as a product of a constant $|(\varepsilon_m - \varepsilon_d)/(\varepsilon_m + 2\varepsilon_d)|^2$ and a normalized Lorentzian distribution function fitted to experimental data. Additionally, they evaluated the absorption coefficient of the semiconductor by summing over all direct excitations and assuming a parabolic band gap of the acceptor semiconductor (51).

The transition's oscillator strength, f, which we can calculate from quantum chemistry codes, is related to $\sigma_A(\omega)$ via (48)

$$f = \frac{2\varepsilon_0 m_e c}{\pi e^2} \frac{\sigma_A(\omega)}{I_A(\omega)} = A \frac{\sigma_A(\omega)}{I_A(\omega)} \tag{S7}$$

$I_A(\omega)$ is the normalized absorption spectrum (s/rad), ε_0 is the permittivity of free space, m_e is the electron rest mass, and e is the electron charge. A is in units of s cm^{-2} rad^{-1} giving a dimensionless f. Therefore, by substituting Eqn. S7 into Eqn. S6, w_{RET} for an acceptor on a spherical metal nanoparticle can be re-written as

$$w_{\text{RET}} = \frac{3\kappa^2}{\pi^2 c^2} \frac{a^6}{R^6} \frac{f}{A} \int \Phi_{sca} \frac{|\varepsilon_d|^2}{\varepsilon_r^2} \left| \frac{\varepsilon_m - \varepsilon_d}{\varepsilon_m + 2\varepsilon_d} \right|^2 \omega^2 I_A(\omega) d\omega \tag{S8}$$

It is clear that w_{RET} is directly proportional to oscillator strength f of the acceptor state, and the spectral overlap $\int |(\varepsilon_m - \varepsilon_d)/(\varepsilon_m + 2\varepsilon_d)|^2 \omega^2 J(\omega) d\omega$. Therefore, RET is maximized at the plasmon resonance peak (when $\varepsilon_m \approx -2\varepsilon_d$ for a spherical metal nanoparticle, where the induced dipole field is much greater than the incident field, E_0), and when the scattering and absorption spectra of the metal and the acceptor state overlap. Note that the field enhancement $|E/E_0|^2$ is proportional to $|(\varepsilon_m - \varepsilon_d)/(\varepsilon_m + 2\varepsilon_d)|^2$, since the induced dipole field is related to the induced dipole moment μ_{LSPR}. For example, for a spherical particle

$$E_{out} = E_0 \hat{x} - \mu_{\text{LSPR}} \left[\frac{\hat{x}}{r^3} - \frac{3x}{r^5} (x\hat{x} + y\hat{y} + z\hat{z}) \right] \tag{S9}$$

E_{out} is the field outside the metal particle, where the first term is the applied field, along $\hat{x}$, while the second term is the induced dipole field, along $\hat{x}, \hat{y}, \hat{z}$ (17, 76).

Note that in Ref. (17), for spheroids (nearly rod-like shapes) μ_{LSPR} takes the form

$$\mu_{\text{LSPR}} = \frac{\alpha E_0}{1 - \frac{2}{3} i k^3 \alpha - \frac{1}{b} k^2 \alpha} \tag{S10}$$

with

$$\alpha = \frac{\varepsilon_m - \varepsilon_d}{\varepsilon_m + \chi \varepsilon_d} \frac{b^3 (1 + \chi) \xi_o^2 + 1}{3\xi_o^2} \tag{S11}$$

$$\chi = -1 - 2 \left[\xi_o^2 - \frac{\xi_o(\xi_o^2 + 1)}{2} \cos^{-1} \left(\frac{\xi_o^2 - 1}{\xi_o^2 + 1} \right) \right]^{-1} \tag{S12}$$

$$\xi_o = (\frac{b^2}{a^2} - 1)^{-1/2} \tag{S13}$$

where a and b are the short and long axes of the spheroid, respectively, and $k = 2\pi/\lambda = \omega/c$ (17). This is derived using Mie theory in conjunction with the modified long wavelength

approximation (MWLA) in which the quasistatic approximation is corrected for the finite wavelength effects (*17*). Thus, a similar expression for w_{RET} can be derived for spheroids that depend on a metal's dielectric properties $[(\varepsilon_m - \varepsilon_d)/(\varepsilon_m + \chi\varepsilon_d)]$, dimensions (*a* and *b*), and the position of the acceptor along the spheroid long axis and its orientation relative to the field (*R* and κ^2).
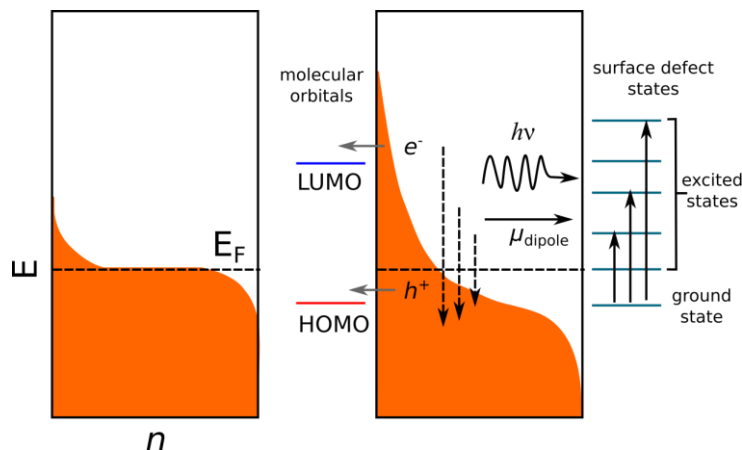

fig. S1. Mechanisms of chemical enhancement on an MNP via an LSPR. Left panel: schematic representation of the population, *n*, of states with energy, E, in a metal near the Fermi level, E_F, at finite temperatures. The electronic population follows a Fermi-Dirac distribution. Right panel: the change in the population distribution after an LSPR excitation. On the left margin, the injection of energetic electrons and holes ("hot" carriers) into the lowest unoccupied (LUMO) and the highest occupied (HOMO) of an adsorbed molecule, respectively, are shown (*23*). On the right margin, defect or adsorbate-induced local surface states showing their excited state spectrum. The LSPR may directly induce an excitation within these states either radiatively or *via* a near-field dipole-dipole interaction: resonance energy transfer (*20, 24*), without necessarily producing excited carriers within the metal.
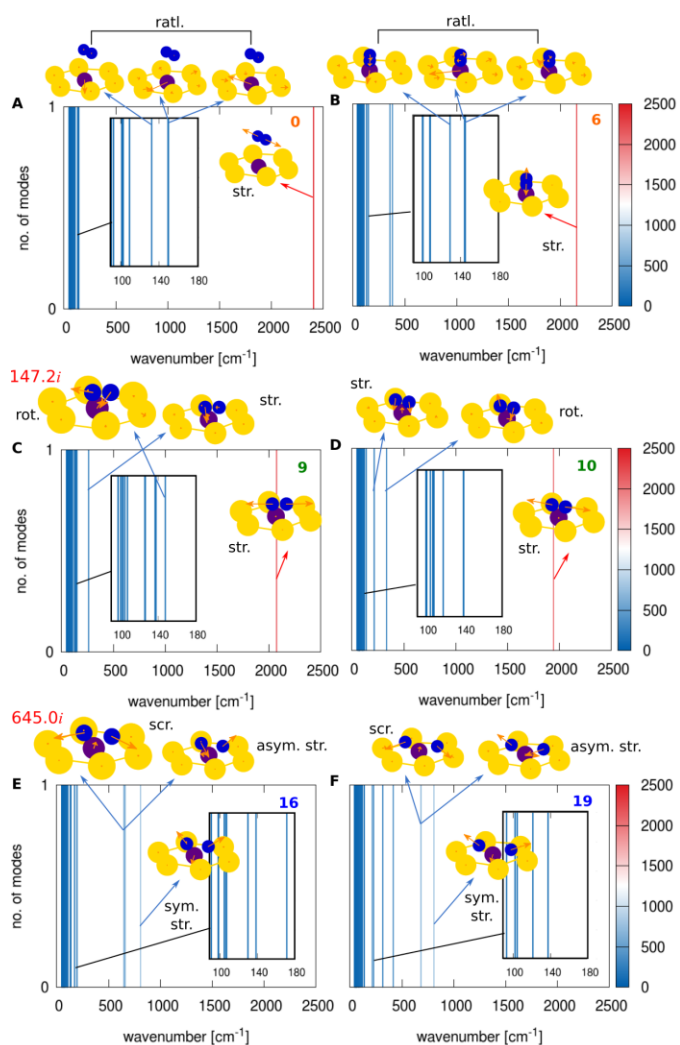
fig. S2. Adsorbate vibrational spectra. Periodic-slab-DFT+D3-calculated ground-state surface vibrational normal modes for critical point structures 0, 6, 9, 10, 16, and 19 shown in Figure 1A of the main text. Structural insets highlight some prominent modes whose eigenvectors ($\times$2, orange arrows) are shown. Yellow circle: Au, violet: Mo, and blue: N. Some of the notable modes are annotated: ratl.: rattle, str.: intramolecular N-N stretch, sym. and asym. str.: N-Mo-N symmetric and asymmetric stretches, rot.: rotation, and scr.: scissoring. C and E correspond to transition state structures 9 and 16; they therefore exhibit non-trivial imaginary frequencies along the reaction coordinate (highlighted accordingly with their frequencies). The aforementioned transition-state modes correspond to instabilities associated with the out-of-plane N_2 rotational mode in C, and N-Mo-N scissoring mode in E. Modes with low frequencies $\lesssim$ 180 cm^{-1} correspond to the unphysical Au_6 vibrations and are the consequence of the truncation of the Hessian matrices to mitigate computational cost. N_2 modes < 100 cm^{-1} (real or imaginary) are taken to be trivial, *e.g.*, gas phase rotational and translational modes. Thus, only the real-valued normal mode frequencies associated with the N and Mo atoms are considered in the ZPE and vibrational free energy calculations for the critical points.
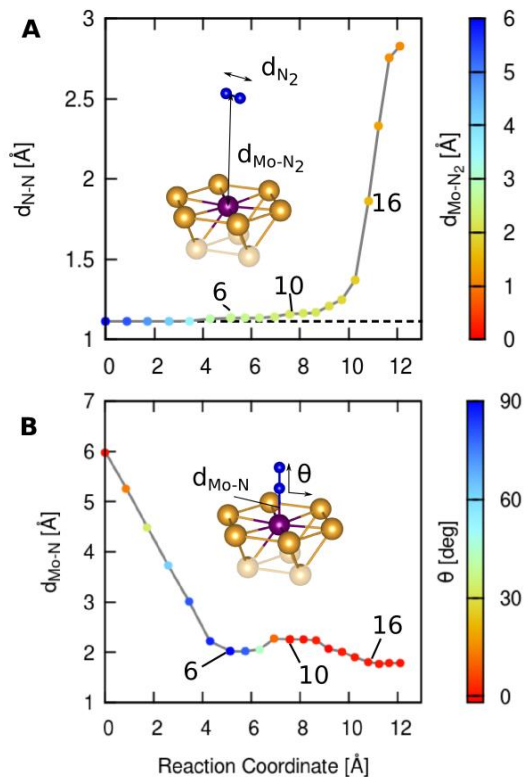
fig. S3. Structural parameters versus reaction coordinate. A. N_2 internal bond length (d_{N-N}) and Mo-to-N_2 center of mass distance (d_{Mo-N2}). B. Distance between the terminal N and Mo (d_{Mo-N}) and angle the molecule makes relative to the in-plane vector (θ).
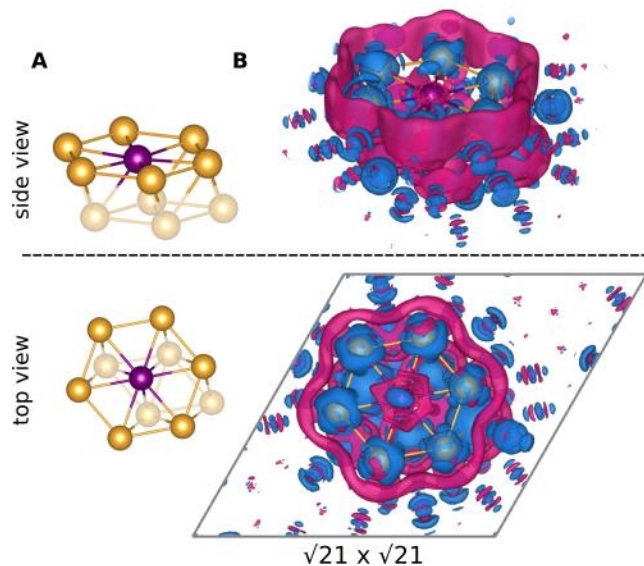
fig. S4. Metal cluster and embedding potential. A. $Au_{10}Mo$ cluster carved out from a $\sqrt{21}\times\sqrt{21}$ five-layer $Au_{104}Mo$ slab (*25, 26*). B. Optimized embedding potential showing negative attractive potential enveloping the cluster and positive repulsive potential near atomic cores. These features allow for the simulation of the severed metallic bonds at the interface of the atoms from the cluster and the Au_{94} environment. Isosurface values: ±1.5 V (blue +, pink −). Yellow sphere: Au, violet: Mo.
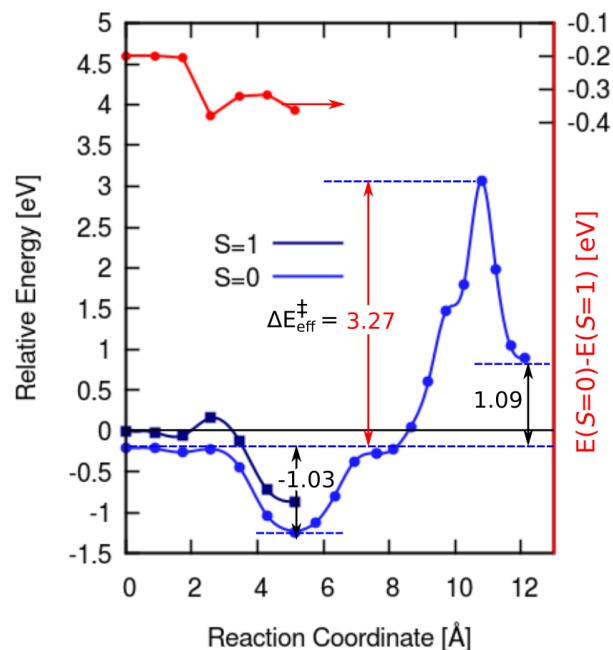
fig. S5. Reaction energy curve using a smaller basis set. The same energy curve as shown in Fig. 1E in the main text, but obtained from the second pre-convergence procedure using a smaller basis set for N and Au (table S1, set 1). This is done to facilitate more efficient convergence at the larger basis (see table S1 for the basis sets used at the different stages of the calculations). The effective barrier and dissociation energy here are predicted to be ~0.2 eV lower than the results obtained using the larger basis set: 3.27 *vs*. 3.48 eV, and 1.09 *vs*. 1.25 eV (as shown in Figure 1E), see also table S2 and S3.

fig. S6. Singlet-triplet energy as a function of embedded metal cluster CAS size. A. *S*=0 *vs*. *S*=1 emb-NEVPT2 energy as a function of the metal cluster CAS size from CAS(6e,6o) to CAS(12e,12o), showing *S*=0 to be the more favorable spin state in all cases (using basis set 2, see table S1). See comment in table S5 regarding even larger CAS sizes. B. CAS(12e,12o) natural orbitals and occupations for *S*=0, left, and *S*=1, right. Orbitals in orange boxes correspond to the CAS(6e,6o), green to (8e,8o), blue to (10e,10o), and violet to (12e,12o). See SM text above for more details.
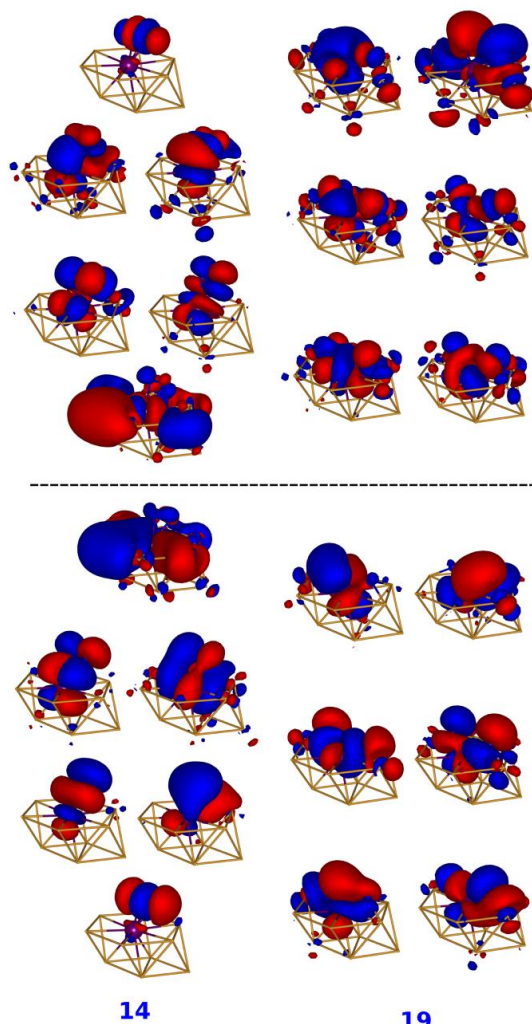
14 **19**

fig. S7. Additional CASSCF natural orbitals. The ground-state CASSCF natural orbitals for structures 14 and 19, demonstrating the changes in the Mo-N_2 bonding interactions (see Figures 1E and 2). The corresponding orbital occupations are in table S4. Orbitals above the black horizontal dashed line are nearly empty (virtual) and below are nearly completely filled (occupied). Isosurface value: 0.02 a.u.; the $Au_{10}Mo$ embedded-cluster model + N_2 are shown, see Figure 1A for structural legend.
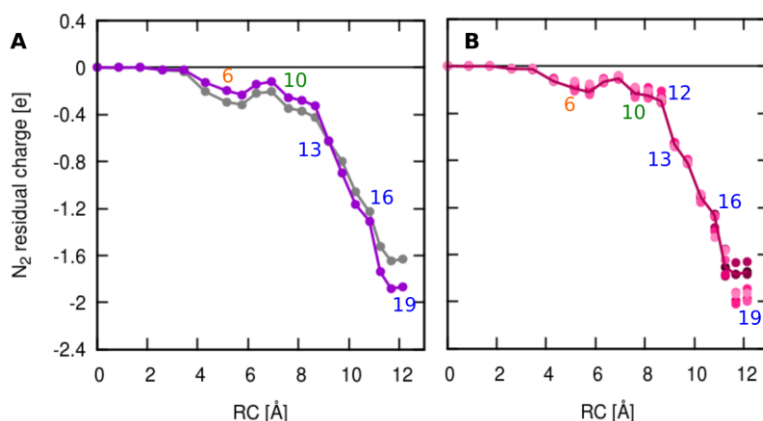
fig. S8. N$_2$ charge versus reaction coordinate. Calculated residual Bader charge on N$_2$ as a function of the reaction coordinate. A. From emb-DFT (gray) and ground-state emb-CASSCF (purple) electron densities. B. For different states (up to the 6th excited state), from the individual electron densities obtained from SA-CASSCF. Line traces the ground-state charges. Emb-CASSCF and emb-DFT differ in their predictions on the amount of charge transferred from the metal cluster onto the molecule, where DFT predicts partial charge-transfer for the physisorbed molecule (η^1-N$_2$ adsorption, structure 6), while emb-CASSCF predicts more charge being transferred beginning at structure 13 where the bond starts to elongate appreciably (fig. S3), until the molecule fully dissociates.
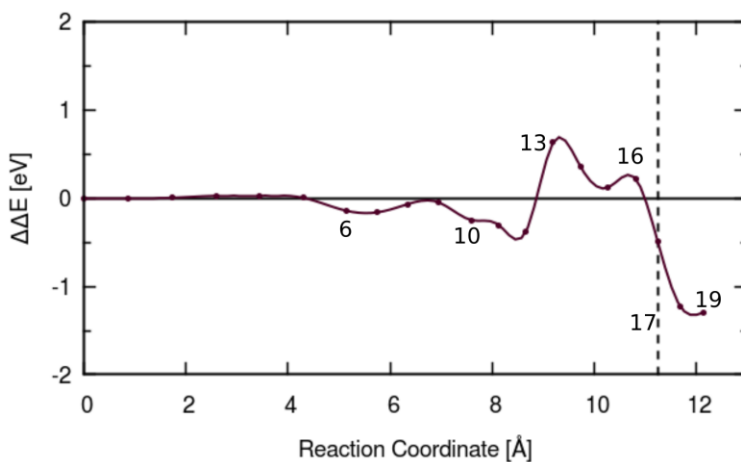
fig. S9. Comparison of the ground-state energy curves predicted by SA-CASSCF and SS-CASSCF. Difference in the ground-state reaction energies predicted by emb-NEVPT2 using ground-state emb-SA-CASSCF and emb-SS-CASSCF reference wavefunctions: ΔE(emb-NEVPT2/emb-SA-CASSCF) – ΔE(emb-NEVPT2/emb-SS-CASSCF). Vertical dashed-line marks s:17, where the energy differences are ~ 0.5 eV for structures that come before and including this structure.
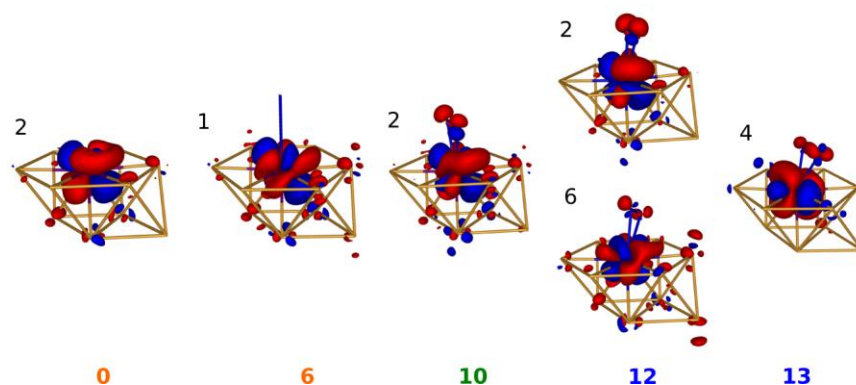
fig. S10. Additional SA-CASSCF(12e,12o) electron difference density plots. Real-space electron difference density plots, calculated by subtracting the ground-state density from the excited-state electron density (as indicated by the adjacent numerical indices, 1: 1st, 2: 2nd excited states, etc.), for structures 0, 6, 10, 12, and 13. Red: electron loss, blue: electron gain, isosurface value: ± 0.002 a.u.; the $Au_{10}Mo$ embedded-cluster model + N_2 is shown, see Figure 1A in the main text for structural legend. The N_2 molecule partially loses an electron in some of these transitions, most notably at the 2nd or 4th excited state for structures 10 to 13. These transitions are also as bright, if not brighter than the transitions to the 5th excited states (see Fig. 3 in the main text), which are instead characterized by partial electron gain in the N_2 molecule.

table S1. GTO basis sets. Basis sets used for the embedded cluster DFT, CASSCF, and NEVPT2 calculations at different stages of the calculations.

Element	Basis set		
	Core Electron Description	Size → Contraction	Common name
set 0: first pre-convergence – ground state CASSCF only			
N	AE	$10s5p2d \rightarrow$ $4s3p2d$	aug-cc-pVDZ (*67*)
Mo	28-electron fully relativistic Stuttgart/Cologne ECP (*68*)	$10s9p8d2f1g \rightarrow$ $5s5p4d2f1g$	cc-pVTZ-PP (*68*)
Au	60-electron fully relativistic Stuttgart/Cologne ECP (*69*)	$8s7p6d \rightarrow$ $4s4p3d$	cc-DZ-PP*
set 1: second pre-convergence and CAS size convergence test			
N	aug-cc-pVDZ (same as set 0)		
Mo	cc-pVTZ-PP (same as set 0)		
Au	same as set 0	$8s7p6d1f \rightarrow$ $4s4p3d1f$	cc-pVDZ-PP (*70*)
set 2: final			
N	AE	$11s6p3d2f \rightarrow$ $5s4p3d2f$	aug-cc-pVTZ (*67*)
Mo	cc-pVTZ-PP (same as set 0)		
Au	same as set 0	$10s9p8d2f1g \rightarrow$ $5s5p4d2f1g$	cc-pVTZ-PP (*70*)
set 3: basis set convergence test			
N	AE	$12s6p3d2f1g \rightarrow$ $5s4p3d2f1g$	cc-pVQZ (*67*)
Mo, Au	cc-pVTZ-PP (same as set 2)		

* modified cc-pVDZ-PP (*70*) where the polarization function *f* is removed

table S2. Benchmark values for the gas-phase N_2 dissociation energy (eV) with respect to the method and basis set used (26). The N_2 bond length is set at 1.114 Å, which is fixed at the equilibrium bond length found using DFT(PBE)-PW to be consistent with the approximation done in the embedded cluster model, while the N-N bond distance for the dissociated case is ~4 Å (25).

N basis set	DFT*†	NEVPT2 from CASSCF(6e,6o) with $2s,2p$ correlated*†‡
aug-cc-pVDZ	10.306 (-0.257, 0.40)	8.781 (-0.790, -1.13)
aug-cc-pVTZ	10.520 (-0.043, 0.61)	9.354 (-0.217, -0.56)
cc-pVQZ	10.562 (-0.001, 0.65)	9.531 (-0.040, -0.38)
aug-cc-pVQZ	10.563 (0.0, 0.65)	9.571 (0.0, -0.34)

*quantities in parentheses: deviation relative to aug-cc-PVQZ and experiment: 9.91 eV removing the zero-point energy correction,(5) (red, black).
†spin-unrestricted S_z=3 or S=3 for the dissociated case
‡the same level of correlation is included as in the embedded cluster model to show the level of accuracy in our adsorption models

table S3. Dependence of reaction energies on basis set. Comparison of the emb-NEVPT2 reaction energies along the MEP (eV/N_2) for S=0 for structure i relative to i=0 for different basis sets.

basis set*	i†			
	6	10	16	19
set 1	-1.032 (-0.117)	-0.071 (-0.137)	3.267 (-0.352)	1.094 (-0.256)
set 2	-1.031(-0.116)	-0.070 (-0.136)	3.478 (-0.141)	1.250 (-0.100)
set 3	-0.915	0.066	3.619	1.350

* see table S1 for the definition of the basis sets
† quantities in parentheses: deviation relative to set 3 (N: cc-pVQZ, Mo: cc-pVTZ, Au: cc-pVTZ).

table S4. Ground-state CAS natural orbital occupations. CAS natural orbitals shown in Figs. 2 and S7.*

Structure						
0	**6**	**10**	**13**	**14**	**16**	**19**
0.02	0.02	0.02	0.02	0.03	0.04	
0.06, 0.06	0.06, 0.05	0.07, 0.04	0.07, 0.02	0.04, 0.03	0.08, 0.07	0.04, 0.02
0.09	0.09	0.08	0.10	0.12, 0.11	0.12, 0.11	0.07, 0.05
0.13, 0.12	0.12, 0.12	0.13, 0.12	0.14, 0.12	0.14	0.25	0.08, 0.08
1.88, 1.87	1.88, 1.88	1.88, 1.86	1.88, 1.85	1.89	1.74	1.93, 1.92
1.91	1.91	1.93	1.92	1.91, 1.91	1.90, 1.88	1.95, 1.94
1.94,1.94	1.94,1.94	1.94, 1.94	1.95, 1.93	1.95, 1.93	1.92	1.97, 1.96
1.98	1.98	1.98	1.98	1.98	1.94, 1.94	

*follows the same orbital order. Above the dashed-line: virtuals, below: occupied.

table S5. Dependence of reaction energies on CAS size. The change in emb-NEVPT2 reaction energies along the MEP (eV/N_2) for $S=0$ for structure i, relative to $i=0$, for different active space sizes.* Here basis set 1 is used (see table S1).

CAS(ne,no) +RAS(me,mo)	No. of reference CSFs	i			
		6	10	16	19
		relative to CAS(12e,12o)			
$n=10$, $m=0$[†]	19,404	-0.172	-0.137	-0.424	-0.338
$n=6$, $m=6$[‡]	189,895	-0.013	-0.019	+0.005	-0.028
$n=4$, $m=8$[‡]	115,420	0.176	-0.139	‖	0.086
$n=4$, $m=10$[§]	591,435	-0.073	0.125	‖	-0.187
		relative to CAS(4e,4o)+RAS(8e,8o)			
$n=4$, $m=10$[§]	591,435	-0.236	0.282	‖	-0.245

*CASSCF CAS(14e,14o) converges successfully, but currently beyond the capability of the NEVPT2 implementation for the size of the system studied here. The number of reference CSFs for CAS(12e,12o) and CAS(14e,14o) are 226,512 and 2,760,615, respectively.

†adsorption and dissociation energies are predicted to be more negative/less positive in CAS(10e,10o) than in the larger CAS(12e,12o). This is in part because of the poorer description of correlation in the N_2 molecule due to the removal of the lowest-energy occupied and highest-energy virtual orbitals: N_2 5σ and $6\sigma^*$ from the CAS (see Figure 2 in the main text for the CAS(12e,12o) natural orbitals).

‡ using orbitals from CASSCF CAS(12e,12o) as initial guess

§ using orbitals from CASSCF CAS(14e,14o) as initial guess

‖ RASSCF nonconvergent: indication of inadequacy of RASSCF in describing the transition state

movie S1. DFT + D3 CI-NEB–predicted structures along pathway *a* (physical adsorption). Images show only the Au_9Mo+N_2 fragment for clarity.

movie S2. DFT + D3 CI-NEB–predicted structures along pathway *b* (reorientation). Images show only the Au_9Mo+N_2 fragment for clarity.

movie S3. DFT + D3 CI-NEB–predicted structures along pathway *c* (dissociation). Images show only the Au_9Mo+N_2 fragment for clarity.

data file S1. Atomic structure files. The zip file contains atomic structure files obtained from slab DFT+D3 CI-NEB, contained in the folder "periodic-slab" (in cif format), and structure files generated for the embedded cluster calculations, contained in the folder "emb-cluster" (in xyz format).